Mon. Not. R. Astron. Soc. **000**, 1–13 () Printed 29 March 2010 (MN LATEX style file v2.2)

The transition from population III to population II-I star formation

Umberto Maio[1,2⋆] Benedetta Ciardi[1], Klaus Dolag[1], Luca Tornatore[3], Sadegh Khochfar[2]
[1]*Max-Planck-Institut für Astrophysik, Karl-Schwarzschild-Straße 1, D-85748 Garching b. München, Germany*
[2] *Max-Planck-Institut für extraterrestrische Physik, Giessenbachstraße 1, D-85748 Garching bei München, Germany*
[3] *Dipartimento di Astronomia dell'Universitá di Trieste, via Tiepolo 11, I-34131 Trieste, Italy*

...(draft)

ABSTRACT

We present results from the first cosmological simulations which study the onset of primordial, metal-free (population III), cosmic star formation and the transition to the present-day, metal-rich star formation (population II- I), including molecular (H_2, HD, etc.) evolution, tracing the injection of metals by supernovæ into the surrounding intergalactic medium and following the change in the initial stellar mass function (IMF) according to the metallicity of the corresponding stellar population. Our investigation addresses the role of a wide variety of parameters (critical metallicity for the transition, IMF slope and range, SN/pair-instability SN metal yields, star formation threshold, resolution, etc.) on the metal-enrichment history and the associated transition in the star formation mode. All simulations present common trends. Metal enrichment is very patchy, with rare, unpolluted regions surviving at all redshifts, inducing the simultaneous presence of metal-free and metal-rich star formation regimes. As a result of the rapid pollution within high-density regions due to the first SN/pair-instability SN, local metallicity is quickly boosted above the critical metallicity for the transition. The population III regime lasts for a very short period during the first stages of star formation ($\sim 10^7\,\mathrm{yr}$), and its average contribution to the total star formation rate density drops rapidly below $\sim 10^{-3} - 10^{-2}$.

Key words: Cosmology:theory - early Universe

1 INTRODUCTION

The standard paradigm of cosmic structure formation relies on the classical approach of Jeans' theory (Jeans 1902) applied to primordial matter fluctuations in the frame of an expanding Universe. Cosmological models for structure formation have been developed since several decades (e.g. Gunn & Gott 1972; Peebles 1974; White & Rees 1978) and the overall picture agrees with a "flat" Universe where "cold-dark matter" is the dominant fraction of matter and the "cosmological constant", Λ, is the dominant fraction of the cosmological energy density. Baryonic structures arise from in-fall and condensation of gas into dark-matter potential wells. In particular, it seems (e.g. Maiolino et al. 2007) that molecular gas could account for a significant fraction of the dynamical mass of early objects. Recent determinations of the cosmological parameters (Komatsu et al. 2010) suggest a present-day expansion rate $H_0 \simeq 70\ \mathrm{km/s/Mpc}$ (in units of $100\ \mathrm{km/s/Mpc}$ this parameter becomes $h \simeq 0.70$), a total-matter density parameter $\Omega_{0m} \simeq 0.272$, with "baryonic" component $\Omega_{0b} \simeq 0.0456$, and a cosmological-constant density parameter $\Omega_{0\Lambda} \simeq 0.728$. The primordial power spectrum of perturbation is well fitted by a power law with index $n \simeq 0.96$ and normalization via mass variance within 8 Mpc/h radius $\sigma_8 \simeq 0.8$. As a reference, it is common to define the standard ΛCDM model the one with the following parameters: $H_0 = 70\ \mathrm{km/s/Mpc}$, $\Omega_{0m} = 0.3$, $\Omega_{0b} = 0.04$, $\Omega_{0\Lambda} = 0.7$, $\Omega_{0tot} = 1.0$, $n = 1$, $\sigma_8 = 0.9$. In the frame of cosmic evolution, it is believed that structure formation takes place from the growth of primordial fluctuations in matter density. These would contract and collapse allowing gas cooling and the subsequent build-up of stars. The determination of the properties of early stars and their effects on the following baryonic-structure formation episodes is still a problem under debate (for a complete review see e.g. Ciardi & Ferrara 2005). Nevertheless, it is reasonably well established that the very first generation of stars should be characterized by massive objects with typical masses much larger than the presently observed ones (Schwarzschild & Spitzer 1953; Woosley & Weaver 1995; Larson 1998; Chiosi 2000; Heger & Woosley 2002, 2008). These primordial stars (population III stars) are formed out of a pristine environment, where the cooling agents are limited to primordial, H-based molecules only, i.e. H_2 and HD, which are able to cool the gas down to temperatures of $\sim 10^2$ K. Therefore, the mass of primordial stars should be relatively large and their spectrum, biased towards such large objects, is commonly referred to as "top-heavy" initial mass function (IMF) (Larson 1998). These features imply very short lifetimes (up to $\sim 10^6$ years only) and final

⋆ E-mail: umaio@mpe.mpg.de, maio@mpa-garching.mpg.de (UM)

death mostly into black holes (Heger & Woosley 2002). The only mass range where primordial stars can explode as pair-instability supernovæ (PISN) and pollute the surrounding medium is [140-260] $M_\odot$ (Heger & Woosley 2002). Nevertheless, also at masses of $\sim 100 - 140\ M_\odot$ there can be some mass loss before collapse (pulsational pair SN). The key uncertainty here is primary nitrogen production and the dredge up of carbon and oxygen. In particular, if the stellar atmosphere is highly CNO enhanced there may be substantial mass loss, but zero metallicity should still be a good first approximation for such stellar flows (S. Woosley, private communication).

Despite the many uncertainties on their characteristics, population III (popIII) stars have an important impact on the evolution of the intergalactic medium (IGM), since they initiate the metal pollution of the IGM, with consequent change of its chemical composition and cooling properties (chemical feedback). Therefore, star formation events in enriched regions will happen in completely different conditions, because metals allow further cooling and fragmentation to smaller scales. This results in an initial stellar-mass function peaked at lower masses, similar to the nowadays observed Salpeter-like IMF (Salpeter 1955) for population II-I (popII-I) stars.

A very debated issue is the understanding of the transition from the primordial popIII star formation regime to the standard popII-I regime. In this respect, there are evidences for the existence of a critical metallicity, Z_{crit}, at which the modalities of star formation allow such transition (Bromm et al. 2001; Schneider et al. 2002): Z_{crit} is the metallicity at which the metal cooling function dominates over the molecular one. In this case, the fragmentation process becomes highly enhanced, but the exact value is not well-established, yet. Different studies suggest discrepant values with Z_{crit} varying between $\sim 10^{-6}\ Z_\odot$ (e.g. Schneider et al. 2006) and $\sim 10^{-3}\ Z_\odot$ (e.g. Bromm & Loeb 2003)[1].

The main uncertainty is the presence of dust at high redshift. To our knowledge, dust is produced and injected in the ISM mainly by the low–mass stars in the AGB phase. This would imply no dust production at very-high redshift, due to "long" stellar lifetimes: a 8 $M_\odot$ star has a life of ~ 0.1 Gyr, comparable with the age of Universe at $z \sim 15 - 20$. None the less, the presence of large amounts of dust and heavy elements has been detected at moderately-high redshift, i.e. at $z > 6$, when the Universe is younger than ~ 1 Gyr (e.g. Bertoldi et al. 2003; Maiolino et al. 2004). This suggests that dust production must have occurred primarily in the ejecta of supernova explosions, which are the final fate of massive, short-lived stars. If, indeed, supernovæ could be able to induce dust production then star formation in the early Universe and the level of Z_{crit} would be strongly influenced, as well. Enrichment by dust would not impact the thermal structure of the IGM, but its presence would alter the whole star formation process. Indeed, when the metallicity of star forming regions is still below $\sim 10^{-6}\ Z_\odot$ the only relevant coolants are molecules, mainly H_2 and HD, while above $\sim 10^{-4}\ Z_\odot - 10^{-3}\ Z_\odot$ gas cooling is fully dominated by metal fine-structure transitions (e.g. Maio et al. 2007) and cloud fragmentation can happen down to sub-solar scales (Bromm et al. 2001; Schneider et al. 2002, 2004). In between, cooling capabilities depends mainly on the amount of metals depleted onto dust grains. The mass content locked into dust grains, almost independently from the exact mass of SNII/PISN progenitor, reaches $2\% - 5\%$ of the parent mass for type-II SN (Kozasa et al. 1991; Todini & Ferrara 2001; Nozawa et al. 2003; Bianchi & Schneider 2007), and $15\% - 30\%$ for PISN (Nozawa et al. 2003; Schneider et al. 2004), in a few hundred days after the beginning of the explosion. Despite the huge difference between the dust mass fractions deriving from SNII and PISN, the dust-to-metal mass ratios (or "depletion factors") turn out to be $\sim 0.3 - 0.7$ in both cases and, for metal poor SNII progenitors with masses of $25\ M_\odot - 30\ M_\odot$, it is up to ~ 1. The natural conclusion is that first massive stars could spread in the early Universe a lot of dust during their final phases (as either SNII or PISN).

In the present work, we aim at investigating the birth of the first stars, the following cosmic metal enrichment from their explosive death and the transition to the standard, presently observed, star formation regime. We focus on how such transition and the associated features are affected by different choices of Z_{crit}, IMF, post-supernova metal yields, star formation density thresholds, box dimension and resolution.

Throughout the paper we will refer to "population III regime" and "population II-I regime" when the metallicity is below or above the critical level, respectively. In addition, we will adopt the standard ΛCDM cosmological model.

The paper is organized as follows: we describe the code and the simulations in Sect. 2, results are given is Sect. 3, and parameter dependence is addressed in Sect. 4 (4.1, 4.2, and 4.3). We discuss and conclude in Sect. 5.

2 SIMULATIONS

The simulations were performed in the frame of the standard ΛCDM cosmological model, by using the Gadget-2 code (Springel 2005). The initial conditions for the reference simulations were generated sampling 0.7 Mpc/h, comoving (but see also discussion on larger boxes in Sect. 4.3) of the cosmic fluid at redshift $z = 100$, with 320^3 particles per gas and dark matter species, having masses of $116\ M_\odot/h$ and $755\ M_\odot/h$, respectively. We perform the numerical simulations including primordial molecular evolution (Maio et al. 2006, 2007; Maio 2008), star formation prescriptions (Maio 2008; Maio et al. 2009), and metal pollution from stars (Tornatore et al. 2007). We choose the stellar IMF according to the value of the gas metallicity Z: if $Z < Z_{crit}$ a top-heavy IMF is assumed, otherwise a Salpeter one.

More in detail, we include in the code the whole set of chemistry reactions leading to molecule creation or destruction and metal pollution, with the corresponding cooling functions. We follow the abundances of the H- and He-based chemistry, involving e^-, H, H^+, H^-, He, He^+, He^{++}; H_2-chemistry following H_2, H_2^+ (Yoshida et al. 2003) and deuterium chemistry with D, D^+, HD, and HeH^+ (Maio et al. 2007). While in principle an arbitrary number of metals can be accounted for by the scheme for metallicity tracking (Tornatore et al. 2007), in this work we focus on C, O, Mg, S, Si, and Fe, since they are the most abundant metals produced during stellar evolution. We assume, as initial chemical composition, a primordial neutral gas with residual electron and H^+ fractions (Galli & Palla 1998) $x_{e^-} \simeq x_{H^+} \simeq 4 \cdot 10^{-4}$, H_2 fraction $x_{H_2} = 10^{-6}$, H_2^+ fraction $x_{H_2^+} = 3 \cdot 10^{-21}$, D fraction $x_D = 3.5 \cdot 10^{-5}$, D^+ fraction $x_{D^+} = 4 \cdot 10^{-9}$, HD fraction $x_{HD} = 7 \cdot 10^{-10}$, HeH^+ fraction $x_{HeH^+} = 10^{-14}$. Individual metals are set to zero initial abundance.

The natural gas evolution, with the initial in-fall into the dark-matter potential wells and the shock-heating phase, is fully self-

[1] We adopt $Z_\odot \simeq 0.0201$ (Anders & Grevesse 1989; Grevesse & Sauval 1998). See, however, Asplund et al. (2009) for a recently updated value of $Z_\odot \simeq 0.0134$

Table 1. Parameters adopted for the simulations.

Model	box side [Mpc/h]	number of particles	mean inter-particle separation [kpc/h]	$M_{gas}[\mathrm{M}_\odot/h]$	$M_{dm}[\mathrm{M}_\odot/h]$	Z_{crit}	$n_{\mathrm{H,th}}$ $[\mathrm{cm}^{-3}]$	popIII IMF range [$\mathrm{M}_\odot$]	Massive yields
Zcrit3	0.7	2×320^3	2.187	1.16×10^2	7.55×10^2	$10^{-3} Z_\odot$	70	[100, 500]	HW02[1]
Zcrit4	0.7	2×320^3	2.187	1.16×10^2	7.55×10^2	$10^{-4} Z_\odot$	70	[100, 500]	HW02[1]
Zcrit5	0.7	2×320^3	2.187	1.16×10^2	7.55×10^2	$10^{-5} Z_\odot$	70	[100, 500]	HW02[1]
Zcrit6	0.7	2×320^3	2.187	1.16×10^2	7.55×10^2	$10^{-6} Z_\odot$	70	[100, 500]	HW02[1]
Zcrit4-r8-100	0.7	2×320^3	2.187	1.16×10^2	7.55×10^2	$10^{-4} Z_\odot$	70	[8, 100]	HW08[2]
Zcrit4-r0.1-100	0.7	2×320^3	2.187	1.16×10^2	7.55×10^2	$10^{-4} Z_\odot$	70	[0.1, 100]	HW08[2]
Zcrit4-HW8-40	0.7	2×320^3	2.187	1.16×10^2	7.55×10^2	$10^{-4} Z_\odot$	70	[0.1, 100]	HW08[2]
Zcrit4-WW8-40	0.7	2×320^3	2.187	1.16×10^2	7.55×10^2	$10^{-4} Z_\odot$	70	[0.1, 100]	WW95[3]
Zcrit4-th7	0.7	2×320^3	2.187	1.16×10^2	7.55×10^2	$10^{-4} Z_\odot$	7	[100, 500]	HW02[1]
Zcrit4-th1	0.7	2×320^3	2.187	1.16×10^2	7.55×10^2	$10^{-4} Z_\odot$	1	[100, 500]	HW02[1]
Zcrit4-th01	0.7	2×320^3	2.187	1.16×10^2	7.55×10^2	$10^{-4} Z_\odot$	0.1	[100, 500]	HW02[1]
Zcrit4-5th7	5.0	2×320^3	15.62	4.23×10^4	2.75×10^5	$10^{-4} Z_\odot$	7	[100, 500]	HW02[1]
Zcrit4-10th7	10.0	2×320^3	31.25	3.39×10^5	2.20×10^6	$10^{-4} Z_\odot$	7	[100, 500]	HW02[1]

[1] Data tables from Heger & Woosley (2002).
[2] Data tables from Heger & Woosley (2008).
[3] Data tables from Woosley & Weaver (1995).

consistently followed through the attainment of the isothermal turnover and the subsequent cooling regime. This stage is very important at early times, as it represents the state when gas cooling balances and takes over heating. Resolving the isothermal phase in primordial-chemistry simulations is fundamental to account for the early molecular cooling of the gas (as already discussed and shown in Maio et al. 2009). For this reason, we assume that stars are formed roughly at the end of the gas cooling process, when a suitable physical density threshold for early star formation of $\sim 10^2\ \mathrm{cm}^{-3}$ (more exactly $70\,\mathrm{cm}^{-3}$) is reached (Maio 2008; Maio et al. 2009). The often used low-density threshold of $\sim 0.1\ \mathrm{cm}^{-3}$ (e.g. Katz et al. 1996) would induce spurious time anticipation of the onset of star formation (Maio et al. 2009). Hereafter, stars evolve and die according to their characteristic lifetimes, possibly expelling newly created metals into the surrounding gas and modifying its cooling properties either at low (e.g. Maio et al. 2007) and at high temperatures (e.g. Sutherland & Dopita 1993; Wiersma et al. 2009; Cantalupo 2010).

For the very first bursts (and those happening in gas of metallicity smaller than Z_{crit}) we adopt a "Salpeter-like" IMF, in the mass range $[100,\ 500]\,\mathrm{M}_\odot$, with a slope of -1.35. The stellar life-times lie between $\sim 3 \cdot 10^6\,\mathrm{yr}$, for the $100\,\mathrm{M}_\odot$ stars, and $\sim 0\,\mathrm{yr}$ (instantaneous death), for the hundreds-solar-masses stars. As mentioned in the Introduction, the relevant mass range for metal pollution is approximatively $[140,\ 260]\,\mathrm{M}_\odot$, because of the formation of PISN. We point out that in our approach each star forming SPH particle can be assimilated to a simple stellar population, with coeval stars formed out from the same environment. Once the particle (i.e. stellar population) metallicity reaches the critical value, Z_{crit}, popII-I star formation is assumed to set in, in place of popIII, and subsequent stars will have masses in the range $[0.1,\ 100]\,\mathrm{M}_\odot$, distributed according to a Salpeter IMF. PopII-I stellar life-times are usually much longer than those of popIII, ranging between $\sim 2 \cdot 10^{10}\,\mathrm{yr}$, for the $0.1\,\mathrm{M}_\odot$ stars, and $\sim 3 \cdot 10^6\,\mathrm{yr}$, for the $100\,\mathrm{M}_\odot$.

Yields of popIII stars (see discussion in Sect. 4.1) are assumed accordingly to Heger & Woosley (2002), while for popII-I stars we follow Woosley & Weaver (1995) for massive stars (SNII), van den Hoek & Groenewegen (1997) for mass loss of low- and intermediate-mass stars, and Thielemann et al. (2003) for SNIa.

In order to describe properly stellar evolution, it is important to take into account feedback effects which deal with those physical processes that are not resolved because of numerical limitations. In our simulations star forming particles are subject to wind kinetic feedback[2] with velocities of $500\,\mathrm{km/s}$. These particles produce metals which are smoothed over the neighbours according to the SPH kernel.

We perform four numerical simulations considering critical metallicities of $Z_{crit} = 10^{-3}Z_\odot, 10^{-4}Z_\odot, 10^{-5}Z_\odot, 10^{-6}Z_\odot$, which span the full range found in the literature (see Introduction). In Sect. 4.1, 4.2, and 4.3 we will also investigate how the results are affected by a different choice for the popIII IMF, the post-supernova yields, the critical star formation threshold and the box dimension/resolution. A schematic description of the simulations is given in Table 1.

3 RESULTS

In this section, we present results related to the early phases of cosmological metal enrichment and the transition from popIII to popII-I regime. The results refer to the $0.7\,\mathrm{Mpc}/h$ side box described in the previous section, with varying Z_{crit}, the most significant parameter in the calculation.

3.1 Metallicity distribution

In order to have a visual representation of the simulations we show maps at redshift $z = 11$ for the projected metallicity distribution

[2] For a different metal/feedback approach, see also treatments based on thermal feedback (e.g. Scannapieco et al. 2005).

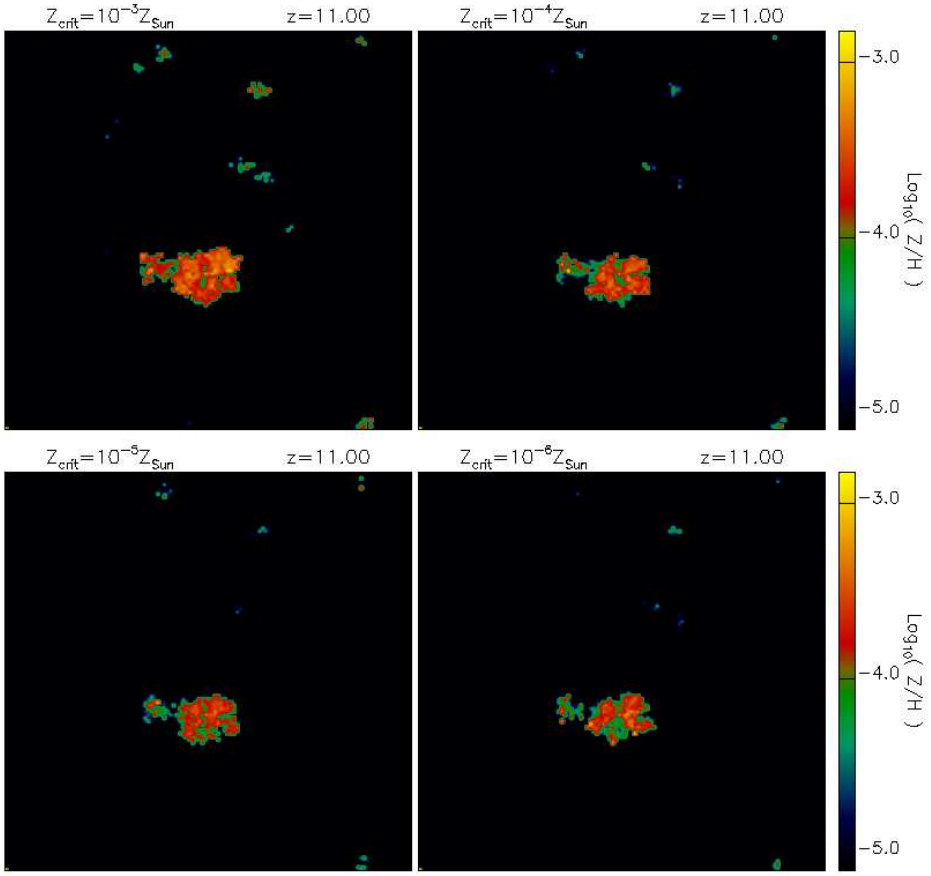

Figure 1. Metallicity maps at redshift $z = 11$ for the $0.7\,\mathrm{Mpc}/h$ side box, with $Z_{crit} = 10^{-3} Z_\odot$ (top-left panel), $10^{-4} Z_\odot$ (top-right panel), $10^{-5} Z_\odot$ (bottom-left panel), and $10^{-6} Z_\odot$ (bottom-right panel). The maps are obtained by projecting the whole simulation box.

(Fig. 1) for all the cases considered: $Z_{crit} = 10^{-3} Z_\odot$ (upper-left panel), $10^{-4} Z_\odot$(upper-right panel), $10^{-5} Z_\odot$(bottom-left panel) and $10^{-6} Z_\odot$ (bottom-right panel). The metallicity is defined as the metal mass fraction of each SPH particle: $Z = m_Z/m_{tot}$, where m_Z and m_{tot} are respectively the mass of metals and the total mass of each SPH particle.

Metal enrichment is very patchy and there are regions which are very strongly polluted and others which preserve their pristine, metal-free composition. The main pollution events happen around the densest regions, where star formation takes place. We stress that the differences in the distribution and level of metallicities are only due to the value of Z_{crit} adopted. In particular, the metallicity of the gas reaches a slightly higher value and wider distribution for the $Z_{crit} = 10^{-3} Z_\odot$ case than for the other cases. This is due to the longer time needed to reach the critical level, Z_{crit}. Once this happens, popII-I star formation sets in and further delays metal pollution, because the SNII from popII-I stars release about one fourth of metals per unit mass than the popIII ones, on a timescale at least ~ 10 times longer. When $Z_{crit} = 10^{-6} Z_\odot$, pollution above the critical metallicity threshold is immediate and most of the regions rapidly move into the popII-I star formation regime. This transition gets delayed as Z_{crit} increases.

In Fig. 2, we compare metal enrichment at different redshifts. The maps refer to $z = 11$ (upper row), 12 (central row) and 13 (bottom row), for $Z_{crit} = 10^{-3} Z_\odot$ (left column) and $10^{-5} Z_\odot$ (right column). The process is quite fast as inferred from the rapid growth of metal-enriched bubbles, and allows for high metal pollution within very short time (see also Sect. 3.2).

To highlight the differences between popIII and popII-I star forming regions, we plot in Fig. 3 the corresponding two-population maps[3] projecting the whole box. They show very well how the star formation regime evolves according to metallicity (see further discussion in Sect. 3.3).

From a more quantitative analysis of the Figure, some distinctive behaviour emerges. For $Z_{crit} = 10^{-6} Z_\odot$, almost all the polluted areas reach the critical metallicity already in $\sim 0.1\,\mathrm{Gyr}$ ($\sim 98\%$ at $z = 13$, $\sim 99\%$ at $z = 12$, and $\sim 100\%$ at $z = 11$). In the other cases we observe a similar quick enrichment: for $Z_{crit} = 10^{-5} Z_\odot, 10^{-4} Z_\odot$ and $10^{-3} Z_\odot$ the percentage of areas with $Z \geqslant Z_{crit}$ is respectively $\sim 72\%$, 49% and 32% at $z = 13$; $\sim 86\%$, 70% and 39% at $z = 12$; and $\sim 99\%$, 97% and 97% at $z = 11$. We note as well that, at fixed redshift, the fraction of popII-I star formation regions decreases with increasing Z_{crit}, because of the higher enrichment level needed to allow the transition from $Z < Z_{crit}$ to $Z \geqslant Z_{crit}$.

As the enrichment process is very localized, also the transition to a different star formation regime strongly depends on location. This means that it is possible to find coexistence of population III and population II-I, with stronger pollution in the central regions of star formation sites and weaker pollution in the outermost ones (see maps in Fig. 1 and in Fig. 2). It is in fact evident that the pref-

[3] In this case, data are not smoothed on the edges of the pixels.

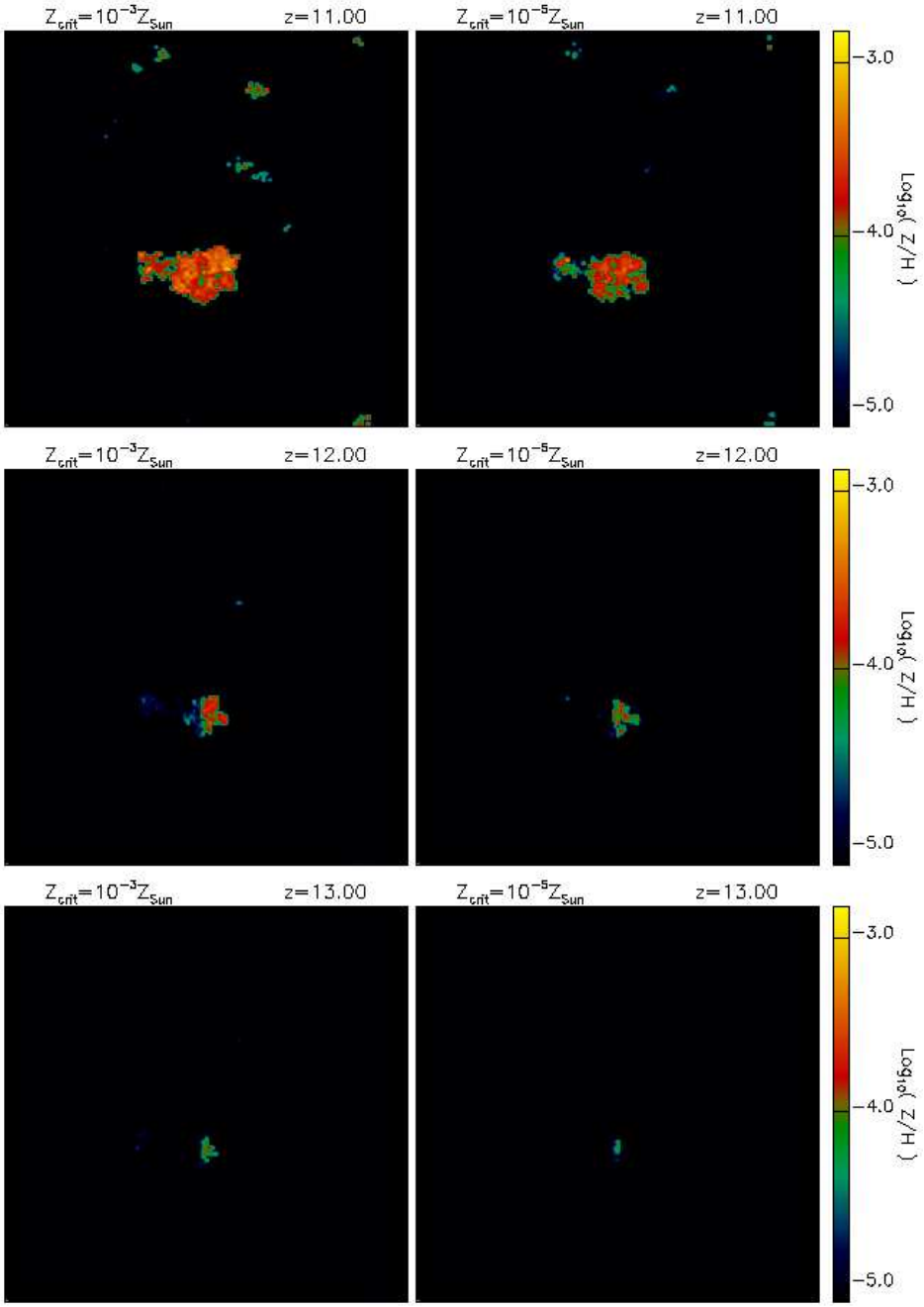

Figure 2. Comparison of the metallicity maps at redshift $z = 11$ (upper row), 12 (central row), and 13 (bottom row), for the $0.7\,\mathrm{Mpc}/h$ side box with $Z_{crit} = 10^{-3} Z_{\odot}$ (left column) and $10^{-5} Z_{\odot}$ (right column). The maps are obtained by projecting the whole simulation box.

erential sites of popIII star formation are isolated areas and often peripheric regions not strongly contaminated by nearby bursts. Our findings are consistent with the study of the $Z_{crit} = 10^{-4} Z_{\odot}$ case by Tornatore et al. (2007). We note that changes in Z_{crit} can only slightly alter the whole enrichment scenario, as just few regions which undergo popII-I star formation for $Z_{crit} = 10^{-5} Z_{\odot}$ are undergoing popIII star formation for $Z_{crit} = 10^{-3} Z_{\odot}$ (e.g. Fig. 3). In fact, accordingly with the previous discussion, the star forming environment is chemically "sterilized" by one or a few subsequent popIII generations.

3.2 Metallicity evolution

From the previous results, it emerges that metal enrichment is a very patchy and inhomogeneous phenomenon. Never the less, as an indicative estimate of the global enrichment history of the Universe, we present the evolution of the average metallicities found in the simulations (Fig. 4). Following previous discussions though, we expect large fluctuations[4] around the mean values reported here. In particular, for each Z_{crit} (labeled on the upper-right corner and

[4] Variances are comparable to the averages.

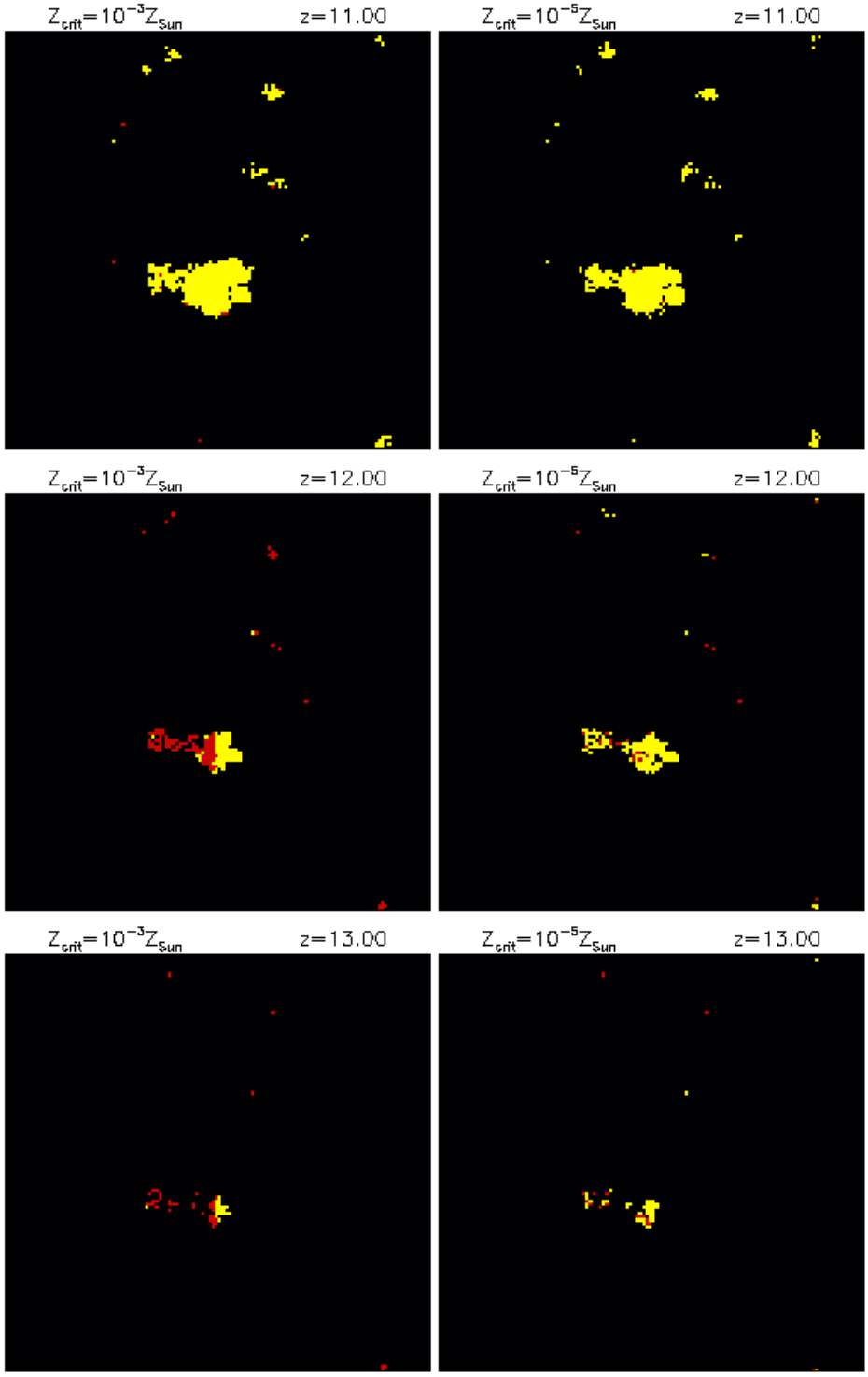

Figure 3. Comparison of the two-population metallicity maps at redshift $z = 11$ (upper row), 12 (central row), and 13 (bottom row), for the $0.7\,\mathrm{Mpc}/h$ side box with $Z_{crit} = 10^{-3} Z_{\odot}$ (left column) and $10^{-5} Z_{\odot}$ (right column). The yellow areas refer to polluted regions with metallicity higher than Z_{crit}, while the red ones to those with metallicity lower than Z_{crit}. The maps are obtained projecting the whole box.

shown by the horizontal dot-dot-dot-dashed line in each panel), we show the maximum metallicity reached at any redshift (dotted lines), the average metallicity of the enriched regions (dot-dashed lines), the average metallicity in the whole simulation box including primordial unpolluted zones (solid line) and the corresponding individual metallicities for the different metals tracked by the code (dashed lines).

The first metals spread during the final stages of stellar evolution leads to typical metallicities in the surrounding ISM of $Z \sim (10^{-5} - 10^{-4})\, Z_{\odot}$, which, shortly after, rise to values of $Z \sim$

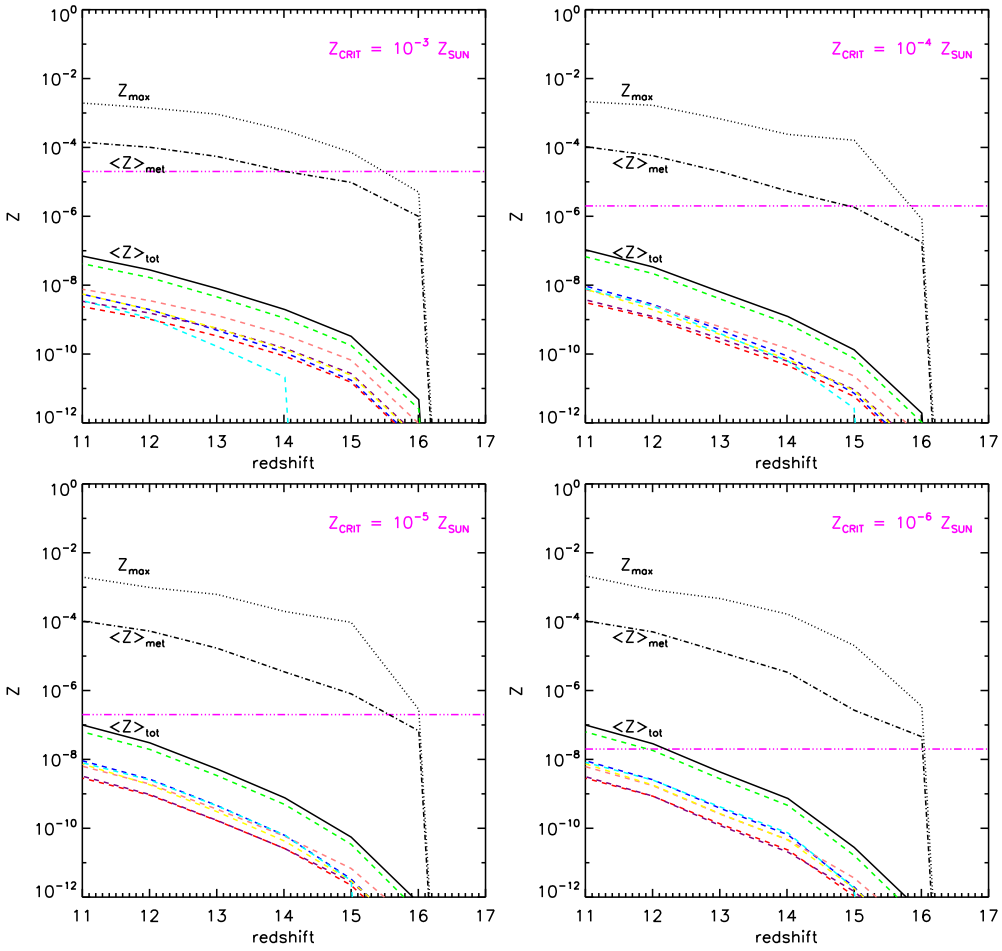

Figure 4. Metal evolution as function of redshift for the $0.7\,\mathrm{Mpc}/h$ side box simulations, with $Z_{crit} = 10^{-3} Z_\odot$ (upper-left panel), $10^{-4} Z_\odot$ (upper-right panel), $10^{-5} Z_\odot$ (bottom-left panel), and $10^{-6} Z_\odot$ (bottom-right panel) case. The magenta horizontal dot-dot-dot-dashed line indicates, in each panel, the critical metallicity; the dotted line is the maximum metallicity; the dot-dashed line is the average metallicity of the spread metals; the solid line is the total metallicity averaged over the whole simulation box and the dashed lines the corresponding individual metallicities: oxygen (green), carbon (blue), magnesium (red), sulphur (purple), silicon (pink), iron (yellow), other metals (cyan) – see also text in Sect. 2.

$(10^{-4} - 10^{-3})\, Z_\odot$, between redshift $z \sim 16$ and $z \sim 15$. Therefore, the critical metallicity Z_{crit} is easily overtaken, despite its precise, actual determination. The leading element is always oxygen, as it is the most abundant one produced by SNII and PISN explosions.

For higher Z_{crit} the popIII regime lasts longer, so that more massive star explosions take place which can pollute the medium up to higher metallicities, before popII-I star formation regime sets in. This results in a quicker Z increase in the very early stages (the difference between the $Z_{crit} = 10^{-3} Z_\odot$ and $Z_{crit} = 10^{-6} Z_\odot$ cases is almost two orders of magnitude at $z \sim 15$).

Broadly speaking, a metallicity of $10^{-6} - 10^{-5}\, Z_\odot$ is locally reached after only $\sim 10^5$ yr. In $\sim 5 \cdot 10^6$ yr, it is possible to get $Z \sim 10^{-4}\, \mathrm{Z}_\odot$ or even $Z \sim 10^{-3}\, \mathrm{Z}_\odot$. An average pollution of $Z \sim Z_{crit}$ is always obtained in a few 10^7 yr (i.e. $\Delta z \sim 1$, at $z \sim 16$) after the onset of star formation (Fig. 4). Once the critical metallicity is reached, popII-I star formation sets in and contributes (on longer timescales) to metal enrichment, as well.

3.3 Star formation from population III and population II-I stellar generations

In Fig. 5, we plot the average[5] popIII star formation rate, $\mathrm{SFR_{III}}$, and the average total star formation rate, $\mathrm{SFR_{tot}}$. For all the simulations the onset of star formation is at $z \simeq 16.3$, when the Universe is about $2.3 \cdot 10^8$ yr old (independently from Z_{crit}, which plays a role only in the following epochs). As shown in Fig. 5, at the very beginning popIII contribution is dominant, but rapidly fades away and the popII-I regime is established.

For the $Z_{crit} = 10^{-3} Z_\odot$ case, the contribution is higher and it decreases with Z_{crit}. In fact, the higher Z_{crit}, the higher the number of star forming regions with $Z < Z_{crit}$. The total star formation rate density is only mildly influenced by the exact value adopted for Z_{crit}, meaning that popIII star formation does not affect the global behaviour significantly and the bulk of star formation is mainly led by popII-I stars. The reason for this is simply understood in terms of timescales, as popIII stars have shorter lifetimes (at most $\sim 10^6$ yr)

[5] The average is the arithmetic average of the star formation rates taken at each time-step and binned over 50 bins in redshift.

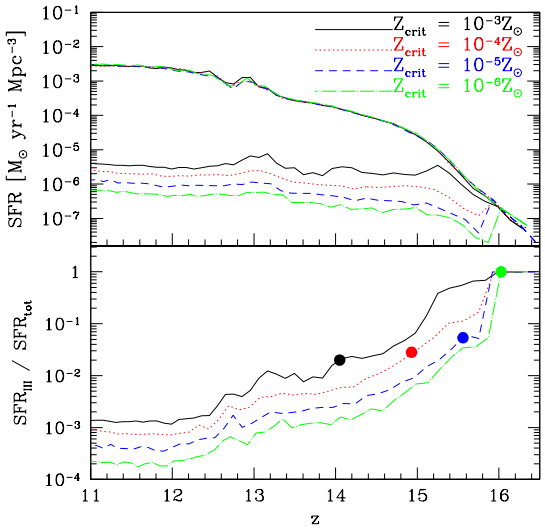

Figure 5. *Upper panel*: redshift evolution of the average star formation rate densities (in $\mathrm{M_\odot yr^{-1} Mpc^{-3}}$) for the $0.7\,\mathrm{Mpc}/h$ side box simulations. The four upper lines are the total star formation rate densities for $Z_{crit} = 10^{-3} Z_\odot$ (solid line), $10^{-4} Z_\odot$ (dotted line), $10^{-5} Z_\odot$ (dashed line), and $10^{-6} Z_\odot$ (dotted-dashed line). The four lower lines are the corresponding popIII contributions. *Bottom panel*: evolution of the ratio between the average popIII star formation rate density ($\mathrm{SFR_{III}}$) and the total star formation rate density ($\mathrm{SFR_{tot}}$), $\mathrm{SFR_{III}/SFR_{tot}}$. The bullets correspond to the redshift at which the average metallicity of the enriched particles equals the value of Z_{crit} (as in Fig. 4).

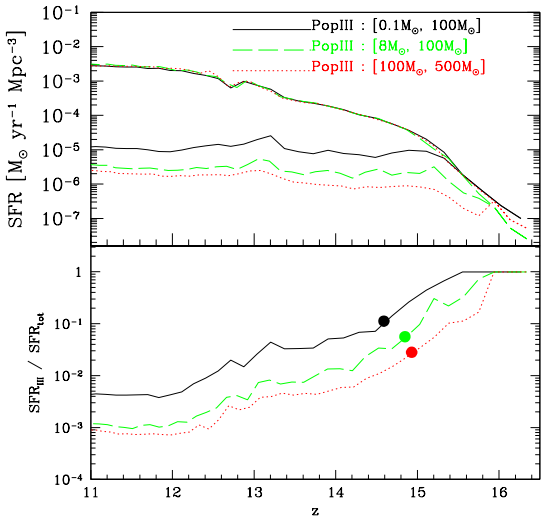

Figure 6. *Upper panel*: redshift evolution of the average star formation rate densities (in $\mathrm{M_\odot yr^{-1} Mpc^{-3}}$) for the $0.7\,\mathrm{Mpc}/h$ side box simulations with $Z_{crit} = 10^{-4} Z_\odot$. The upper lines are the total star formation rate densities for different popIII IMF mass range: $[0.1\ \mathrm{M_\odot}, 100\ \mathrm{M_\odot}]$ (solid lines), $[8\ \mathrm{M_\odot}, 100\ \mathrm{M_\odot}]$ (dashed lines), and $[100\ \mathrm{M_\odot}, 500\ \mathrm{M_\odot}]$ (dotted lines). The lower lines are the corresponding popIII contributions. *Bottom panel*: evolution of the ratio between the average popIII star formation rate density ($\mathrm{SFR_{III}}$) and the total star formation rate density ($\mathrm{SFR_{tot}}$), $\mathrm{SFR_{III}/SFR_{tot}}$. The bullets correspond to the redshift at which the average metallicity of the enriched particles equals the value of Z_{crit}.

and heavily pollute the medium up to Z_{crit} via PISN explosions. Therefore, after the first bursts, it is much easier to match the conditions for standard popII-I star formation, rather than metal free star formation. The period over which star formation is dominated by popIII is slightly longer in the $Z_{crit} = 10^{-3} Z_\odot$ case and decreases gradually with Z_{crit}. For $Z_{crit} = 10^{-3} Z_\odot$, $\sim 100\%$ of the total SFR is due to popIII stars in the redshift interval $z \sim 15 - 16$ (equivalent to a time interval of $\sim 2 \cdot 10^7$ yr), while the percentage decreases to an average value of roughly 0.1% at $z \sim 12$. In the $Z_{crit} = 10^{-6} Z_\odot$ case, there is a sudden drop below $\sim 10\%$ already at $z \sim 15 - 16$ and down to $\sim 0.01\%$ at $z \sim 12$. The intermediate cases are bracketed by the former two regimes. These trends are consistent, because the time to pollute the IGM to lower Z_{crit} is shorter. The resulting behaviour – the smaller Z_{crit}, the earlier the transition from popIII to popII-I dominated star formation – is expected, because, as mentioned, the time needed to pollute the IGM up to lower Z_{crit} is shorter.

The dots on the lines of the average fractions of popIII star formation rate densities, point to the redshifts when the average enrichment reaches the level of Z_{crit} (i.e. the abscissa of the intersecting point between the dotted line and the horizontal line in each panel of Fig. 4) for the different cases. At those redshifts, the average contribution of popIII star formation has already dropped of more than one order of magnitude. For the $Z_{crit} = 10^{-6} Z_\odot$ case, Z_{crit} is reached in the polluted regions when $\mathrm{SFR_{III}/SFR_{tot}} \sim 1$ and this ratio steeply decreases afterwards. In the cases with higher Z_{crit}, the popII-I regime develops simultaneously with the popIII regime, and the average popIII contribution to the total star formation rate when $Z \sim Z_{crit}$ is below $\sim 10\%$.

4 PARAMETER DEPENDENCE

In the following, we will investigate the effects on our results of the main parameters (other than Z_{crit}) adopted in the simulations and choose as reference the one with box dimension $0.7\,\mathrm{Mpc}/h$, $Z_{crit} = 10^{-4} Z_\odot$, $n_{\mathrm{H,th}} = 70\,\mathrm{cm^{-3}}$ and Salpeter slope for popIII stars in the range $[100\mathrm{M_\odot}, 500\mathrm{M_\odot}]$. We have also checked the effects of adopting a different implementation of SPH (the relative pressure SPH, *rp*SPH, according to Abel 2010), which only considers pressure gradients in force calculations and performes closer to grid-based codes. We found no strong deviations in the general gas state (as also expected from the discussion in Sect. 3.8 of Abel 2010) and even in the star formation rates. Metal pollution at early times is slightly more scattered, due to the capability of the *rp*SPH implementation of better resolving instabilities. Overall, there are no substantial changes in our results.

4.1 Different population III IMF's and yields

In order to account for the uncertainties on the popIII IMF, we explore first the role of the slope of the popIII IMF, which so far has been fixed to the value $s = -1.35$.

There are no robust arguments (neither theoretical nor observational) supporting the above assumption and different slopes or shapes are not excluded. None the less, by changing slope, the expected fraction of PISN is not dramatically modified, as its value is always around ~ 0.4 for any s between roughly -1 and -3. Thus, the results on metallicity evolution and star formation rates are not altered at all.

Differently, the chosen mass range and yields of popIII stars could

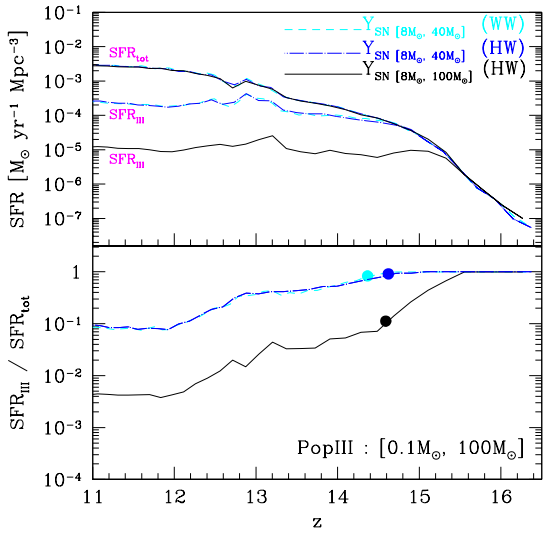

Figure 7. *Upper panel*: redshift evolution of the average star formation rate densities (in $\mathrm{M_\odot yr^{-1} Mpc^{-3}}$) for the $0.7\,\mathrm{Mpc}/h$ side box simulations with $Z_{crit} = 10^{-4} Z_\odot$. The upper lines are the total star formation rate densities for different popIII metal yields, and fixed the popIII IMF mass range at $[0.1\ \mathrm{M_\odot}, 100\ \mathrm{M_\odot}]$: primordial SN yields for stars of $[8\ \mathrm{M_\odot}, 40\ \mathrm{M_\odot}]$ (case Z=0 in Woosley & Weaver 1995) (dashed lines), primordial SN yields for stars of $[8\ \mathrm{M_\odot}, 40\ \mathrm{M_\odot}]$ (Heger & Woosley 2008) (dot-dashed lines), and primordial SN yields for stars of $[8\ \mathrm{M_\odot}, 100\ \mathrm{M_\odot}]$ (Heger & Woosley 2008) (solid lines). The lower lines are the corresponding popIII contributions. *Bottom panel*: evolution of the ratio between the average popIII star formation rate density ($\mathrm{SFR_{III}}$) and the total star formation rate density ($\mathrm{SFR_{tot}}$), $\mathrm{SFR_{III}/SFR_{tot}}$. The bullets correspond to the redshift at which the average metallicity of the enriched particles equals the value of Z_{crit}.

play a more important role, since they directly affect metal pollution and star formation history. The existence of popIII stars with masses below $\sim 10^2\ \mathrm{M_\odot}$ is supported by numerical simulations (e.g. Yoshida 2006; Yoshida et al. 2007; Campbell & Lattanzio 2008; Suda & Fujimoto 2010), which find that it is possible to fragment primordial clouds down to $\sim 10\ \mathrm{M_\odot}$. According to Woosley & Weaver (1995), $Z = 0$ massive stars can die as SN if their mass is smaller than $40\ \mathrm{M_\odot}$; above this limit, they collapse into black holes. Recent updates, though, suggest that such stars can die as SN even if their masses are larger, up to $100\ \mathrm{M_\odot}$ (Heger & Woosley 2008). We have investigated the implications of the uncertainties on our results.

In Fig. 6, together with the results for our reference run (dotted lines), we show the trends for different popIII IMF mass ranges (while we keep the same slope), assuming metal yields for primordial, massive SN from Heger & Woosley (2008)[6]. We plot star formation rates and the corresponding popIII contribution for popIII IMF mass ranges of: $[0.1\ \mathrm{M_\odot}, 100\ \mathrm{M_\odot}]$ (solid lines), $[8\ \mathrm{M_\odot}, 100\ \mathrm{M_\odot}]$ (dashed lines), and $[100\ \mathrm{M_\odot}, 500\ \mathrm{M_\odot}]$ (dotted lines). The latter case is our reference run and its popIII contribution is always lower than the other ones. The reason is the extremely short lifetime of stars with masses in the range $[100\ \mathrm{M_\odot}, 500\ \mathrm{M_\odot}]$ (and in particular in the PISN range), which pollute the surrounding medium in a time-lag much shorter than the one needed to longer-living $\sim 10\ \mathrm{M_\odot}$ stars. Therefore, metal pollution and the transition to popII-I regime happen earlier, with a residual popIII contribution of a factor of 3 or 4 smaller. The difference between the extreme case of stellar masses in the range $[0.1\ \mathrm{M_\odot}, 100\ \mathrm{M_\odot}]$ and the case of stellar masses in the range $[8\ \mathrm{M_\odot}, 100\ \mathrm{M_\odot}]$ is simply due to the different normalization of the IMF, since yields and massive-SN lifetimes are the same. Indeed, the SN fractions are ~ 0.14 and 1, respectively. Thus, as in the latter case 100% of the stars dies as SN, their enrichment results slightly higher, and the popIII contribution drops faster than in the former one (see also the bullets in the lower panel).

Finally, we investigate the effects of different metal yields, according to Woosley & Weaver (1995) and Heger & Woosley (2008). As the massive-SN mass range differs in the two works, in order to have a fair comparison between the yields only and to exclude normalization effects, we fix the popIII IMF range as $[0.1\ \mathrm{M_\odot}, 100\ \mathrm{M_\odot}]$ and the massive-SN mass range as $[8\ \mathrm{M_\odot}, 40\ \mathrm{M_\odot}]$. In Fig. 7, we compare the results for the Woosley & Weaver (1995)'s yields (dashed lines) and for the Heger & Woosley (2008)'s ones (dot-dashed lines). For sake of completeness, we re-plot also the results for the IMF mass range of $[0.1\ \mathrm{M_\odot}, 100\ \mathrm{M_\odot}]$ and the massive-SN range of $[8\ \mathrm{M_\odot}, 100\ \mathrm{M_\odot}]$ (Heger & Woosley 2008). Due to the longer lifetimes of $10\ \mathrm{M_\odot} - 40\ \mathrm{M_\odot}$ stars (dashed lines and dot-dashed lines), with respect to PISN and $100\ \mathrm{M_\odot}$ star lifetimes (solid lines), the popIII regime can now last longer (compare bullets in Fig. 7 with the ones in Fig. 5 or in Fig. 6), and contribute up to 10% the total SFR at $z \sim 11$: some order of magnitude more than all the other cases. By directly comparing the effects of adopting different yields, in the same mass range, it comes out that their impact is negligible and there are no significant changes in the star formation history.

4.2 Density threshold for star formation

We now address how the transition from popIII to popII-I depends on the choice of the density threshold for star formation. Indeed, it is usual to assume that star formation takes place only in converging flows where a given number density is reached. Because different thresholds lead to different onsets of star formation (see also Maio et al. 2009), this could also affect the properties of the transition. For this reason, we re-run the reference simulation ($n_{\mathrm{H,th}} = 70\,\mathrm{cm^{-3}}$) assuming density thresholds of $n_{\mathrm{H,th}} = 7, 1, 0.1\,\mathrm{cm^{-3}}$. Also in these cases the enrichment is very fast and the critical level in polluted environments is always reached between redshifts ~ 15 and 18, very close to the value of our fiducial case, ~ 15 (see Fig. 4). Obviously, the higher the density threshold the later the onset of star formation, as the gas needs more time to condense.

In Fig. 8 we show the star formation rates and the contribution from popIII stars for different density thresholds. The asymptotic amplitude of the total SFR is not affected, but the contribution from popIII stars has different slopes for different $n_{\mathrm{H,th}}$: the higher the threshold, the steeper the evolution of $\mathrm{SFR_{III}/SFR_{tot}}$, with this ratio decreasing of ~ 3 orders of magnitude in redshift intervals of $\Delta z \sim 15$, 8, 6, 4, for $n_{\mathrm{H,tr}} = 0.1$, 1, 7, 70, respectively.

It is evident that the difference between the $70\,\mathrm{cm^{-3}}$, $7\,\mathrm{cm^{-3}}$, and $1\,\mathrm{cm^{-3}}$ cases is quite small, with star formation rates almost overlapping since the beginning of the process. The reason is that such values fall in correspondence of the gas cooling branch, which is extremely fast and therefore the effects on the final results are

[6] We use the tabulated post-supernova yields (Table 8 in Heger & Woosley 2008) for the $10\ \mathrm{M_\odot} - 100\ \mathrm{M_\odot}$ stars, explosion energy of 1.2 Bethe, standard mixing prescriptions, S=4 piston parameter (S. Woosley, private communication).

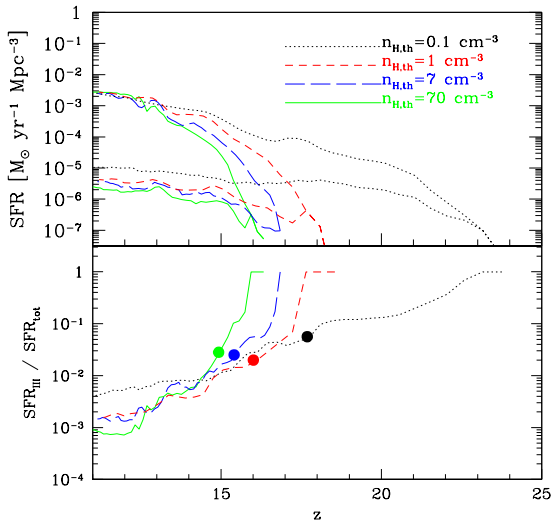

Figure 8. *Upper panel*: redshift evolution of the average star formation rate densities (in $\mathrm{M_\odot yr^{-1} Mpc^{-3}}$) for the $0.7\,\mathrm{Mpc/h}$ side box simulations with $Z_{crit} = 10^{-4} Z_\odot$. The upper lines are the total star formation rate densities for different H-density thresholds for star formation, $n_{\mathrm{H,th}} = 0.1\,\mathrm{cm^{-3}}$ (dotted lines), $1\,\mathrm{cm^{-3}}$ (short-dashed lines), $7\,\mathrm{cm^{-3}}$ (long-dashed lines), and $70\,\mathrm{cm^{-3}}$ (solid lines). The four lower lines are the corresponding popIII contributions. *Bottom panel*: evolution of the ratio between the average popIII star formation rate density ($\mathrm{SFR_{III}}$) and the total star formation rate density ($\mathrm{SFR_{tot}}$), $\mathrm{SFR_{III}/SFR_{tot}}$. The bullets correspond to the redshift at which the average metallicity of the enriched particles equals the value of Z_{crit}.

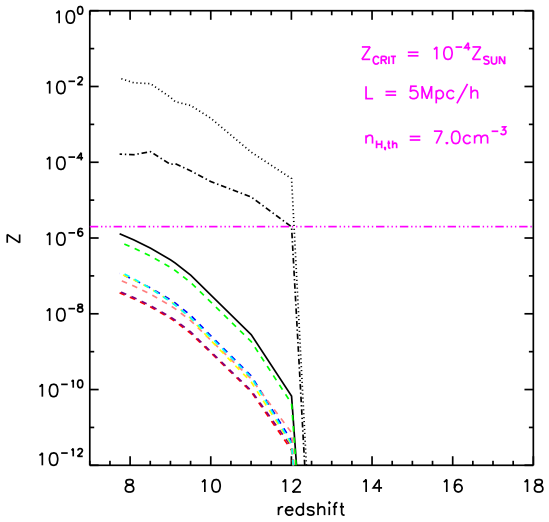

Figure 9. Average metallicities in the simulation of the box with a comoving side length of 5 Mpc/*h* and $Z_{crit} = 10^{-4} Z_\odot$. The density threshold is $7\,\mathrm{cm^{-3}}$. The magenta horizontal dot-dot-dot-dashed line indicates the critical metallicity; the dotted line is the maximum metallicity; the dot-dashed line is the average metallicity of the spread metals; the solid line is the total metallicity averaged over the whole simulation box; and the dashed lines the corresponding individual metallicities (see also Fig. 4).

very little. For the $0.1\,\mathrm{cm^{-3}}$ case, instead, we find discrepancies at higher redshift due to the unresolved isothermal peak. This is due to the fact that (unphysical) low-density threshold models convert gas into stars quite regularly and smoothly, when it is still shock-heating in the hosting dark-matter potential well. But, if high-density thresholds are used, the dense gas is converted into stars later on, only after the loitering, isothermal phase (during which it just gets accumulated at temperatures around $\sim 10^4$ K) and the catastrophic run-away cooling. So, large amounts of particles undergo star formation in a shorter time, after which the SFR catches up and converges to the low-density-threshold cases. In the meantime, the critical metallicity is more quickly reached, as well. This also explains the differences among the slopes of the decrement. The higher the density thresholds, the higher the gas accumulated and catastrophically converted into stars, the higher the enrichment, and the steeper the ratio $\mathrm{SFR_{III}/SFR_{tot}}$.

The popIII/popII-I transition (see bullets) happens in all the cases when the contribution of $\mathrm{SFR_{III}}$ has dropped roughly between $10^{-2} - 10^{-1}$, and at redshift $z \sim 10$ it is $\sim 10^{-3}$.

These conclusions support the fact that the transition from popIII to popII-I star formation regime is very fast, independently from the detailed numerical parameters, as long as the gas isothermal phase is resolved.

4.3 Box size

In this section, we discuss the effect on our results of different choices for the box size. In the next, we will show metallicity properties (Sect. 4.3.1) and star formation rate densities (Sect. 4.3.2) for simulations with the same parameters used for our reference simulation but with a box size in comoving units of $5\,\mathrm{Mpc}/h$ and $10\,\mathrm{Mpc}/h$. Properties and resolution are also summarized in Table 1. Because of the lower resolution of such boxes (gas particle masses are of the order $\sim 10^4 - 10^5 \mathrm{M_\odot}/h$), we cannot adopt a very-high-density threshold (of $\sim 10^2\,\mathrm{cm^{-3}}$ or more), therefore, to make a meaningful comparison we show results for $n_{\mathrm{H,th}} = 7\,\mathrm{cm^{-3}}$.

4.3.1 *Metallicity*

The global behaviour is patchy and similar to the maps already shown for the $0.7\ \mathrm{Mpc}/h$ cases (Figs. 1, 2, 3). The only difference is the larger sampling of star forming regions with a wider statistical significance.

In Figs. 9 and 10, we plot metallicity evolution for the simulations with 5 Mpc/*h* and 10 Mpc/*h* box side, respectively. In both cases, the critical metallicity is reached quite quickly and metal-rich regions have $Z > Z_{crit}$ already by redshift ~ 10. The rapid attainment of Z_{crit} is independent of the resolution, which instead influences the onset of star formation. That is the reason why, in the 10 Mpc/*h* box side, star formation is slightly delayed. As in Fig. 4, we also plot the maximum (dotted lines) and average metallicity in the whole simulation box (solid lines) with the different metal contributions (dashed lines). We find that the first can easily reach solar values, because of strong pollution due to the high PISN metal yields; the second has $Z < Z_{crit}$ at any redshift above ~ 7. These fluctuations are reflected in the high patchiness of early metal spreading. The metal pollution histories do not show large discrepancies and, in spite of differences in resolution of more than one order of magnitude for the SPH masses, an overall agreement between larger (5 or 10 Mpc/*h*) and smaller (0.7 Mpc/*h*) boxes is

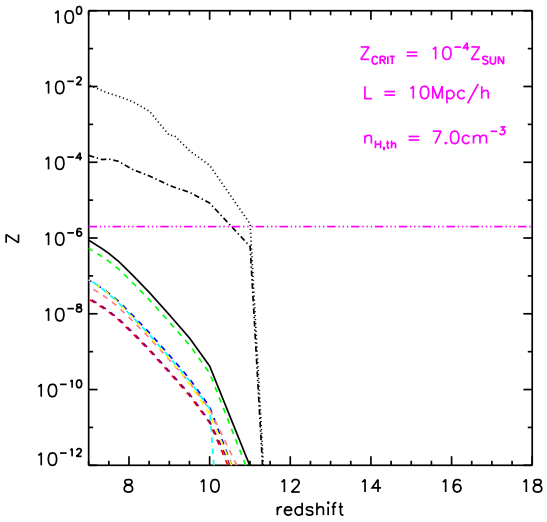

Figure 10. Average metallicities in the simulation of the box with a comoving side length of 10 Mpc/*h* and $Z_{crit} = 10^{-4} Z_{\odot}$. The density threshold is $7\,\mathrm{cm}^{-3}$. The magenta horizontal dot-dot-dot-dashed line indicates the critical metallicity; the dotted line is the maximum metallicity; the dot-dashed line is the average metallicity of the spread metals; the solid line is the total metallicity averaged over the whole simulation box and the dashed lines the corresponding individual metallicities (see also Fig. 4).

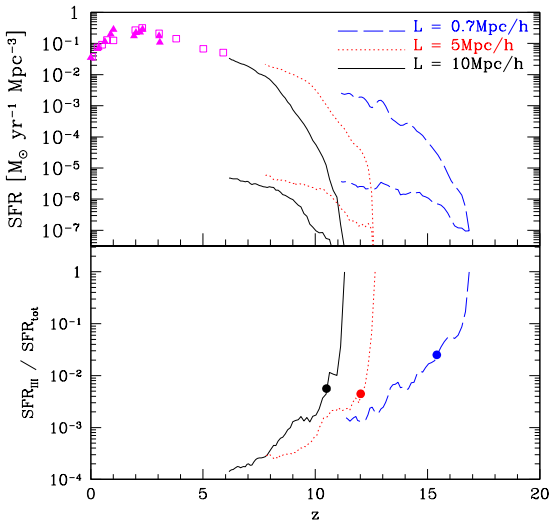

Figure 11. *Upper panel*: star formation rate densities for the simulations with a comoving box side of $0.7\,\mathrm{Mpc}/h$ (dashed lines), $5\,\mathrm{Mpc}/h$ (dotted lines) and $10\mathrm{Mpc}/h$ (solid lines). The density threshold is $7\,\mathrm{cm}^{-3}$. For each of them, we show the total star formation rate density (upper lines) and the popIII one (lower lines). Data points (Reddy et al. 2008) are different determinations of the star formation rate density: square symbols are the UV determinations, triangular symbols are the IR determinations. *Bottom panel*: evolution of the ratio between the average popIII star formation rate density ($\mathrm{SFR_{III}}$) and the total star formation rate density ($\mathrm{SFR_{tot}}$), $\mathrm{SFR_{III}/SFR_{tot}}$. The bullets correspond to the redshift at which the average metallicity of the enriched particles equals the value of Z_{crit}.

reached. Thus, the general results are independent from the particular cosmological sampling.

4.3.2 Star formation from population III and population II-I stellar generations

We will now discuss the behaviour of the star formation rates for the simulations previously introduced.

The average star formation rate densities are shown in the upper panel of Fig. 11, for the boxes of $0.7\,\mathrm{Mpc}/h$ (dashed lines), $5\,\mathrm{Mpc}/h$ (dotted lines), and $10\,\mathrm{Mpc}/h$ (solid lines). The upper lines refer to the total star formation rate densities and the ones below to the corresponding popIII star formation rate densities (data points are by Reddy et al. 2008). Overall, they seem to connect fairly well with the observed trend at lower redshift.

In the bottom panel, we present the ratios of popIII versus total star formation rate. Independently from the box size, the popIII contribution is unity at the very beginning (i.e. $\sim 100\%$ of the SFR is due to popIII) and, for all the cases, rapidly decreases below $\sim 1\%$ at redshift $z \sim 11$, and below $\sim 0.1\%$ at redshift $z \lesssim 11$: a time-lag much shorter than a Gyr. This means, consistently with what said in Sect. 3, that the bulk of popIII episodes happpens in a short time after the onset of star formation and it dominates the cosmological SFR for a limited period at high redshift. At lower redshift, only isolated regions could still have pristine environment and host popIII star formation (which is none the less several order of magnitude smaller that the total SFR).

A general feature of the large box simulations is the slight delay of the onset of star formation: this is due to the limited capabilities of the bigger SPH particles to condense, cool, and collapse. Indeed, molecular cooling is not efficient when the SPH masses are so high ($\sim 10^4 - 10^5 \mathrm{M}_{\odot}/h$) and the primordial gas in-fall is not well resolved. The qualitative agreement of these results is encouraging, though.

5 DISCUSSION AND CONCLUSIONS

In this work, we perform numerical simulations of early structure formation, including both primordial, molecular evolution and metal enrichment from stellar death, to study the transition from an early, massive star formation mode to a more standard one, regulated by the gas metallicity. We follow (see details in Maio et al. 2007; Tornatore et al. 2007) the abundances of e^-, H, H^+, H^-, He, He^+, He^{++}, H_2, H_2^+, D, D^+, HD, HeH^+, C, O, Mg, S, Si, Fe, and use different initial stellar-mass functions, metal yields, and critical metallicities for the transition from a popIII to a popII star formation mode, Z_{crit}. At the present, our work is the only one dealing with detailed chemical evolution, from early molecule creation to the later stages of star formation, and, at the same time, allowing to trace simultaneous, different stellar populations, according to the underlying metallicity.

Indeed, early structure formation can be accurately modeled only with a proper treatment of both the chemistry of primordial molecules and the metal enrichment. In fact, the main influence of chemical evolution on the following generations of structures is via metal pollution (chemical feedback). This event can completely alter the cooling properties of the gas and thus the modalities of star formation, inducing a transition from a top-heavy to a standard IMF. The transition is believed to happen when the gas is enriched above Z_{crit}, which allows fragmentation below the typical scales determined by primordial molecular cooling. Because of

our ignorance of the features of early dust formation and the lack of precision of many atomic and molecular data, the exact determination of Z_{crit} is still elusive; reasonable values should range between $10^{-6}\,Z_{\odot}$ and $10^{-3}\,Z_{\odot}$ (Bromm et al. 2001; Schneider et al. 2002).

In our simulations we assume four different values of Z_{crit} in the above range: $10^{-6}, 10^{-5}, 10^{-4}$, and $10^{-3}\,Z_{\odot}$. From our investigation, some common features emerge. In general, metal pollution, independently from the parameters adopted in the simulations, is very patchy, with excursions of orders of magnitudes at all redshifts. This is consistent with any simulation including metal enrichment (Raiteri et al. 1996; Gnedin 1998; Mosconi et al. 2001; Lia et al. 2002a,b; Kawata & Gibson 2003; Kobayashi 2004; Ricotti & Ostriker 2004; Scannapieco et al. 2005; Tornatore et al. 2007; Oppenheimer et al. 2009). In addition, the gas is easily enriched above Z_{crit}. For this reason, the average contribution from pristine, metal-free (or $Z < Z_{crit}$) stars to the total cosmic star formation density is dominant only in the very early phases of structure formation, while it drops below $\sim 10^{-3}$ quite rapidly, after the explosion of the first pair-instability supernovæ and their metal ejection. In fact, PISN explosions which follow the death of the first, metal-free or very-metal-poor stars, are the main responsibles for enriching the surrounding medium up to a minimum level of $\sim 10^{-4}\,Z_{\odot}$. This means that nearby star forming regions have a very high probability of being polluted above Z_{crit} (as seen also in Fig. 4), while popIII star formation can still occur farther away, in rare, isolated regions with pristine or low-metallicity gas (e.g. Fig. 3). None the less, this would not be the dominant star formation regime.

Our findings hold regardless of the value of Z_{crit}, the popIII IMF adopted, and the numerical parameters involved in modeling star formation (as shown in Sect. 4.1, 4.2, and 4.3). Differences are found if different IMF mass ranges for primordial stars are used. Because of the short life and the high metal yields of early, massive SN, the popIII regime contributes, in any case, only slightly to the global SFR (as expected by e.g. Ricotti & Ostriker 2004), since the early pollution events quickly raise Z above Z_{crit}, independently from the detailed prescriptions.

The simulations were performed using a standard ΛCDM cosmology, but slightly different parameters would not change the general picture. We have checked this, by running simulations with $\Omega_{0m} = 0.26$, $\Omega_{0\Lambda} = 0.74$, $\Omega_{0b} = 0.0441$, $h = 0.72$, $\sigma_8 = 0.796$, and $n = 0.96$ (WMAP5 data, Hinshaw et al. 2008) and found that the same results hold, albeit shifted by a $\Delta z \sim$ of a few to lower redshift (because of the smaller Ω_{0m}).

One last comment about the role of dust production from SNII and/or PISN: one of the main uncertainties in determining Z_{crit}. According to our findings, given the strength and rapidity of metal enrichment (see e.g. Figs. 4, 9 and 10), details about dust and its impact on Z_{crit} are not relevant for the general process and for our understanding of the transition from primordial, popIII regime to present-day-like, popII-I regime (even if they could be of some interest on very local scales). The entire process, in fact, is dominated by metal pollution and the strong yields of early, massive stars.

We have to stress some *caveats*, though. Ejection of particles into the IGM is an unknown process. We have assumed winds originated from stars (kinetic feedback), but different mechanisms (like gas stripping, shocks, thermal heating from stellar radiation, etc.) could play a role, as well, mostly at high redshifts, when objects are small and can easily loose part of their baryonic content. In addition, diffusion and conduction will probably alter the smoothness of metal and molecule distribution, but these phenomena have not been extensively studied, yet, and probably will depend on many parameters: e.g., the way metal or gas particles are ejected and mixed, how they are transferred away from the production sites, how strong is the efficiency of such processes, just to mention a few. Some attempts to address such issues have been done (Spitzer 1962; Cowie & McKee 1977; Brookshaw 1985; Sarazin 1988; Monaghan 1992; Cleary & Monaghan 1999; Klessen & Lin 2003; Jubelgas et al. 2004; Monaghan et al. 2005; Wadsley et al. 2008; Greif et al. 2009), but much more realistic and detailed analyses are still strongly needed.

To conclude, we have followed the structure formation process from very early times to first star formation and subsequent metal pollution. In the 1 Mpc side box simulations we have seen that, after $\sim 2 \times 10^8$ yr, molecular evolution leads the very first bursts of star formation (popIII), but metal enrichment is extremely fast (Figs. 1, 2, and 3) in inducing the nowadays observed star formation mode (popII-I). In fact, we observe a steep increase of Z, with local values rapidly reaching and overtaking Z_{crit} (Fig. 4). Metal pollution proceeds from the densest cores of star formation outwards, because of supernova ejections from high-density to lower-density environments (Figs. 2, and 3). Rare, unpolluted regions can still survive, determining the simultaneous presence of the two star formation regimes, and Z_{crit} can affect the level of residual popIII star formation. As a result of this rapid pollution, we find that the average contribution of the popIII component to the total star formation rate density is of a few times $\sim 10^{-4} - 10^{-3}$ (with a maximum of $\sim 10^{-2} - 10^{-1}$) at $z \sim 11$ (Figs. 5,6, and 7). This general picture is preserved regardless of the precise value of the metallicity threshold Z_{crit} the slope of the popIII IMF, and their yields, but is quite sensitive to the popIII mass range. The change of the critical density threshold for star formation influences little these conclusions, but can affect the onset and the decrement of the popIII contribution to the total SFR (e.g. Fig. 8). We have found similar results in larger-box simulations, either in the metal enrichment features (Figs. 9 and 10) and in the star formation behaviour (Fig. 11).

ACKNOWLEDGMENTS

U. M. wishes to thank useful discussions with Claudio Dalla Vecchia, Massimo Dotti, Jarrett Johnson, Raffaella Schneider, and Stan Woosley. He also thanks Naoki Yoshida and the travel support from the Grant-in-Aid for Scientific Research (S) 20674003 by Japan Society for the Promotion of Science. The simulations were performed by using the machines of the Max Planck Society computing center, Garching (Rechenzentrum-Garching). For the bibliografic research we have made use of the tools offered by the NASA ADS, and by the JSTOR Archive.

More detailed maps and information can be found at the URL http://www.mpe.mpg.de/ umaio/maps.html.

REFERENCES

Abel T., 2010, ArXiv e-prints

Anders E., Grevesse N., 1989, Geochimica et Cosmochimica Acta, 53, 197

Asplund M., Grevesse N., Sauval A. J., Scott P., 2009, ArXiv e-prints

Bertoldi F., Carilli C. L., Cox P., Fan X., Strauss M. A., Beelen A., Omont A., Zylka R., 2003, A&A, 406, L55

Bianchi S., Schneider R., 2007, MNRAS, 378, 973

Bromm V., Ferrara A., Coppi P. S., Larson R. B., 2001, MNRAS, 328, 969
Bromm V., Loeb A., 2003, Nature, 425, 812
Brookshaw L., 1985, Proceedings of the Astronomical Society of Australia, 6, 207
Campbell S. W., Lattanzio J. C., 2008, A&A, 490, 769
Cantalupo S., 2010, MNRAS, 403, L16
Chiosi C., 2000, in Weiss A., Abel T. G., Hill V., eds, The First Stars Evolution of Pop III Stars. pp 95–+
Ciardi B., Ferrara A., 2005, Space Science Reviews, 116, 625
Cleary P. W., Monaghan J. J., 1999, Journal of Computational Physics, 148, 227
Cowie L. L., McKee C. F., 1977, ApJ, 211, 135
Galli D., Palla F., 1998, A&A, 335, 403
Gnedin N. Y., 1998, MNRAS, 294, 407
Greif T. H., Glover S. C. O., Bromm V., Klessen R. S., 2009, MNRAS, 392, 1381
Grevesse N., Sauval A. J., 1998, Space Science Reviews, 85, 161
Gunn J. E., Gott J. R. I., 1972, ApJ, 176, 1
Heger A., Woosley S. E., 2002, ApJ, 567, 532
Heger A., Woosley S. E., 2008, ArXiv e-prints
Hinshaw G., Weiland J. L., Hill R. S., 18 co-authors 2008, ArXiv e-prints, 803
Jeans J. H., 1902, Phil. Trans., 199, A p.1+
Jubelgas M., Springel V., Dolag K., 2004, MNRAS, 351, 423
Katz N., Weinberg D. H., Hernquist L., 1996, ApJS, 105, 19
Kawata D., Gibson B. K., 2003, MNRAS, 340, 908
Klessen R. S., Lin D. N., 2003, Phys. Rev. E, 67, 046311
Kobayashi C., 2004, MNRAS, 347, 740
Komatsu E., Smith K. M., Dunkley J., Bennett C. L., Gold B., Hinshaw G., Jarosik N., Larson D., Nolta M. R., Page L., 11 coauthors 2010, ArXiv e-prints
Kozasa T., Hasegawa H., Nomoto K., 1991, A&A, 249, 474
Larson R. B., 1998, MNRAS, 301, 569
Lia C., Portinari L., Carraro G., 2002a, MNRAS, 335, 864
Lia C., Portinari L., Carraro G., 2002b, MNRAS, 330, 821
Maio U., 2008, Dissertation, LMU Munich: Faculty of Physics, pp 1–229
Maio U., Ciardi B., Yoshida N., Dolag K., Tornatore L., 2009, A&A, 503, 25
Maio U., Dolag K., Ciardi B., Tornatore L., 2007, MNRAS, 379, 963
Maio U., Dolag K., Meneghetti M., Moscardini L., Yoshida N., Baccigalupi C., Bartelmann M., Perrotta F., 2006, MNRAS, 373, 869
Maiolino R., Neri R., Beelen A., Bertoldi F., Carilli C. L., Caselli P., Cox P., Menten K. M., Nagao T., Omont A., Walmsley C. M., Walter F., Weiß A., 2007, A&A, 472, L33
Maiolino R., Schneider R., Oliva E., Bianchi S., Ferrara A., Mannucci F., Pedani M., Roca Sogorb M., 2004, Nature, 431, 533
Monaghan J. J., 1992, ARA&A, 30, 543
Monaghan J. J., Huppert H. E., Worster M. G., 2005, Journal of Computational Physics, 206, 684
Mosconi M. B., Tissera P. B., Lambas D. G., Cora S. A., 2001, MNRAS, 325, 34
Nozawa T., Kozasa T., Umeda H., Maeda K., Nomoto K., 2003, ApJ, 598, 785
Oppenheimer B. D., Davé R., Kereš D., Fardal M., Katz N., Kollmeier J. A., Weinberg D. H., 2009, ArXiv e-prints
Peebles P. J. E., 1974, ApJ, 189, L51+
Raiteri C. M., Villata M., Navarro J. F., 1996, A&A, 315, 105
Reddy N. A., Steidel C. C., Pettini M., Adelberger K. L., Shapley A. E., Erb D. K., Dickinson M., 2008, ApJS, 175, 48
Ricotti M., Ostriker J. P., 2004, MNRAS, 350, 539
Salpeter E. E., 1955, ApJ, 121, 161
Sarazin C. L., 1988, X-Ray Emissions from Clusters of Galaxies, Cambridge Univ. Press., 76, 639
Scannapieco C., Tissera P. B., White S. D. M., Springel V., 2005, MNRAS, 364, 552
Schneider R., Ferrara A., Natarajan P., Omukai K., 2002, ApJ, 571, 30
Schneider R., Ferrara A., Salvaterra R., 2004, MNRAS, 351, 1379
Schneider R., Omukai K., Inoue A. K., Ferrara A., 2006, MNRAS, 369, 1437
Schwarzschild M., Spitzer L., 1953, The Observatory, 73, 77
Spitzer L., 1962, Physics of Fully Ionized Gases, New York: Interscience (2nd edition), 1962. Spitzer L.
Springel V., 2005, MNRAS, 364, 1105
Suda T., Fujimoto M. Y., 2010, MNRAS, pp 444–+
Sutherland R. S., Dopita M. A., 1993, ApJS, 88, 253
Thielemann F.-K., Argast D., Brachwitz F., Hix W. R., Höflich P., Liebendörfer M., Martinez-Pinedo G., Mezzacappa A., Panov I., Rauscher T., 2003, Nuclear Physics A, 718, 139
Todini P., Ferrara A., 2001, MNRAS, 325, 726
Tornatore L., Borgani S., Dolag K., Matteucci F., 2007, MNRAS, 382, 1050
Tornatore L., Ferrara A., Schneider R., 2007, MNRAS, 382, 945
van den Hoek L. B., Groenewegen M. A. T., 1997, A&A Supp., 123, 305
Wadsley J. W., Veeravalli G., Couchman H. M. P., 2008, MNRAS, 387, 427
White S. D. M., Rees M. J., 1978, MNRAS, 183, 341
Wiersma R. P. C., Schaye J., Smith B. D., 2009, MNRAS, 393, 99
Woosley S. E., Weaver T. A., 1995, ApJS, 101, 181
Yoshida N., 2006, New Astronomy Review, 50, 19
Yoshida N., Abel T., Hernquist L., Sugiyama N., 2003, ApJ, 592, 645
Yoshida N., Omukai K., Hernquist L., 2007, ApJ, 667, L117